Supporting Information

Experimental

Molecular beam experiments were performed at the Fritz-Haber-Institut (Berlin) in a UHV apparatus described elsewhere.[S1] An effusive doubly differentially pumped multi-channel array source operated at room temperature was used to supply the D_2 at beam fluxes of 3.2×10^{15} molecules·cm^{-2}s^{-1}. A supersonic beam was used to dose the *cis*-2-butene (Aldrich, >99%) at a flux of 5.6×10^{12} molecules·cm^{-2}s^{-1}. An automated quadrupole mass spectrometer (QMS) system (ABB Extrel) continuously monitored the partial pressure of the reactants (2-butene, C_3H_5 fragment detected at 41 a.m.u.) and products (2-butene-d_1, C_3H_4D fragment at 42 a.m.u.; butane-d_2, $C_3H_5D_2$ fragment at 45 a.m.u.). The QMS data were corrected for the natural abundance of ^{13}C.

Figure S1 shows the evolution of reaction products resulting from *cis-trans* isomerization and hydrogenation of *cis*-2-butene over Pd(111) with D_2 supplied in the course of reactions. The isomerization pathway includes only the first half-hydrogenation step of 2-butene to a butyl surface intermediate and requires only surface-adsorbed H(D) species.[5] Essentially constant isomerization rate in Fig. S1 implies independence of the concentration of surface alkyl species on the presence of subsurface H.[S2] In the hydrogenation pathway, an additional second half-hydrogenation step of the butyl-intermediate leads to the formation of butane. The rate of this step crucially depends on the concentration of subsurface H(D) species in Pd(111) and Pd NPs, as demonstrated by the combination of pulsed molecular beam experiments and resonant Nuclear Reaction Analysis for hydrogen depth profiling.[5,S3] As a consequence, the *cis-trans* isomerization rate can be maintained in the steady-state regime on Pd(111), while hydrogenation rate vanishes because of the depletion of subsurface H(D) reservoir.[S3,S4] However, on Pd NPs (edges of which were modified to facilitate the formation of H^{sub}) it was possible to maintain the hydrogenation in a steady state.[5,S3,S4]

Note that even under the following conditions of alkene hydrogenation on Pd: pressure 10^{-3}-1 bar, temperature ca. 350 K, hydrogen to hydrocarbon ratio 1:1 - 9:1, Teschner et al. could not verify the formation of Pd-C phase.[S5] Our conditions were notably milder (10^{-9} bar, 280 K, hydrogen to hydrocarbon ratio ~600:1), which renders unlikely formation of significant amounts of subsurface C in our experimental setup.

Computational

The calculations were carried out with the plane-wave based Vienna *ab initio* simulation package (VASP)[S6,S7] using the generalized-gradient approximation (GGA) in the form of the exchange-correlation functional PW91.[S8] The interaction between atomic cores and electrons was described by the projector augmented wave (PAW) method.[S9,S10] Except for systems containing Pd and Pt, all calculations are spin-polarized, because our tests have shown negligible spin-polarization effects on Pd and Pt for the purpose of the present study. Test calculations taking dispersion interactions into account using DFT-D2 method[S 11] as implemented in VASP revealed only minor (1-2 kJ mol^{-1}) influence on the ethyl and butyl hydrogenation barrier. For more details of calculations see Ref. [S12].

The enthalpy values required for calculations of Gibbs free energies were obtained from the total energy values (E_{el}) corrected for the internal vibrational energy (E_v)[S13] (including zero-point vibrations (ZPE)) derived from frequency calculations of the optimized structures: $H_{298} = E_{el} + E_v + ZPE$.

The entropy values of the reactants and transition states (TS) include only the vibrational degrees of freedom (S_v), since the adsorbates are bound to the surface sufficiently strongly and the rotational and translational degrees of freedom are converted into vibrations.[S14,S15] Hence, the frustrated rotational and translational modes of the ethyl and hydrogen species were accounted for as a part of the vibrational component of the partition function: $S_{298} = S_v$. Since ethane molecule in the final state structures interacts weakly with the substrate, translational (S_t) and rotational (S_r) degrees of freedom of ethane were additionally taken into account:[S15] $S_{298}(ethane) = S_v + S_t + S_r$, as a component of the total Gibbs free reaction energy ΔG_{298}. The expressions of all enthalpy and entropy contributions can be found elsewhere.[S13] The Gibbs free energy for butyl hydrogenation is calculated in the same way.

TS structures have been located by applying the dimer[S 16] or the climbing-image nudged elastic band[S17,S18] methods. In the latter case we used eight images of the system to form a discrete approximation of the path between fixed end-points. The TS structures obtained in this way were refined until the forces on atomic centers were all below 0.2 eV nm^{-1}. With a normal-mode analysis, we verified for each TS that there is exactly one mode with an imaginary frequency that corresponds to the relevant C-H bond breaking or formation. The reported binding energy values E_b of the adsorbed ethyl and/or adsorbed/absorbed H species were calculated as $E_b = E_{a+s} - E_a - E_s$. Here, E_a is the total (spin-polarized ground-state) energy of the adsorbate(s) in the gas phase (1/2 of H_2 molecule for hydrogen); E_s is the total

energy of the metal substrate (bare or containing pre-ad(ab)sorbed atoms) and E_{a+s} is the total energy of the substrate with all the adsorbates in the optimized geometry. With this definition, negative E_b values indicate a favorable interaction, i.e. energy release during the process under scrutiny.

Description of the employed models

Single-crystal M(111), M = Pd, Pt, Ni, Rh surfaces were modeled by a five-layer slab with a (3×3) surface unit cell, where the three "top" layers were allowed to relax whereas the "bottom" two layers were fixed at the theoretical Pd-Pd, Pt-Pt, Rh-Rh, and Ni-Ni distance of 280, 282, 272, 249 pm, respectively.[S19] The vacuum spacing between adjacent slabs was larger than 1 nm. All the calculations were carried out using a 5×5×1 Monkhorst-Pack k-point grid.[S20]

The employed NP model is a truncated octahedron M_{79} (M = Pd, Pt, Ni, Rh) with fcc structure, which exhibits {111} facets together with very small {100} facets. For Pd, this NP has been shown to enable essentially size-converged (with respect to extended systems) quantification of both structural and energetic observables for species adsorbed on their facets,[S21] which is also supported by the results of the present study. M_{79} species has been positioned in a cubic cell with the lattice parameter 2 nm, which ensures vacuum spacing of ~1 nm between atoms in the neighboring periodically repeated cells. Calculations of the discrete particles have been performed at the **Γ** point in the reciprocal space.

Note that in each of the calculated models at least two vacant adsorption sites are present: one of them to accommodate the reactant ethylene molecule and another nearby site to adsorb an attacking H^{ad} atom that hydrogenates ethylene to ethyl. Thus, H^{ad} coverage at the reaction site is somewhat lower than the saturation hydrogen monolayer coverage.

Effect of the geometric structure on the activity

Increased H loading, indeed, has an effect on the structure of the considered Pd nanoparticle and leads to the elongation of Pd-Pd distances. The diameter of the bare Pd_{79} NP, ~1.15 nm, increases by about 40 pm in *surface-saturated* NP and by additional ~20 pm when subsurface H atoms are added. In order to examine whether the structural changes are responsible for high activity of the *subsurface-saturated* NP, we calculated the Gibbs energy barrier using the *subsurface-saturated* NP with coordinates of Pd atoms fixed at the values for the optimized *surface-saturated* NP. As the calculated value for that model, 5 kJ mol^{-1}, is the same as the barrier for the completely relaxed *subsurface-saturated* NP, we may assume that the changes in the structural parameters of the Pd NP are not responsible for the increased

hydrogenation activity.

As activation energies of ethyl hydrogenation decrease in the presence of subsurface H, the structures of respective TSs change too. One can clearly monitor these changes by focusing on the distance between the attacking H^{ad} atom and attacked C atom of the ethyl in the TSs. When subsurface H is introduced on slabs this distance increases by mere 7 pm, while in the case of Pd_{79} increase of the C-H distance is 17 pm (Table S1). This shows that introducing subsurface H makes the transition state "earlier" (i.e., closer to co-adsorbed ethyl and H^{ad}). This effect is much stronger in the case of Pd_{79} nanoparticle, where strong decrease of activation energy is also calculated. Also, one can note a similar trend in activation energies and TS structures of Pd NP models with varying amount of subsurface H. Models with increasing number of H^{sub} atoms, $H^{ad}{}_{78}H^{sub}{}_{0} \rightarrow H^{ad}{}_{23}H^{sub}{}_{3} \rightarrow H^{ad}{}_{38}H^{sub}{}_{12} \rightarrow H^{ad}{}_{78}H^{sub}{}_{24}$ exhibit decreasing activation barriers $29 \rightarrow 28 \rightarrow 9 \rightarrow 5$ kJ mol^{-1}, respectively. In the same order the TSs become more early (Table S1), with gradual elongation of the forming C-H bond in this sequence: $165 \rightarrow 167 \rightarrow 179 \rightarrow 182$ pm. These findings are in line with Hammond postulate[S22] stating that earlier transition states are generally characteristic of more rapid exothermic reactions.

Table S1. Activation and reaction energies, $\Delta E^{\neq}$ and ΔE, at 0 K as well as distances r from the attacking atom H^{ad} to the nearest atom C or atom Pd (Ni), to which adsorbed ethyl species is bound in the initial state (IS) and transition state (TS) structures of the reaction $C_2H_5 + H \rightarrow C_2H_6$ on the models of metal catalysts depicted in Figure 1.[a]

Model	$\Delta E^{\neq}$ kJ mol^{-1}	ΔE kJ mol^{-1}	r^{IS}(C-H) pm	r^{TS}(C-H) pm	r^{IS}(Pd-H) pm	r^{TS}(Pd-H) pm
Nanoparticle						
low-coverage	54	-13	271	157	186	170
surface-saturated	46 (43)	-52 (-55)	263 (256)	165 (159)	187 (170)	171 (159)
subsurface-saturated	16 (58)	-98 (-22)	246 (293)	182 (164)	177 (171)	172 (159)
Single crystal						
low-coverage	50	-26	269	160	185	170
surface-saturated	41 (26)	-54 (-82)	256 (240)	163 (164)	182 (165)	172 (158)
subsurface-saturated	37 (31)	-75 (-66)	257 (250)	170 (162)	180 (165)	171 (159)

[a] Data for the Ni models are given in parentheses.

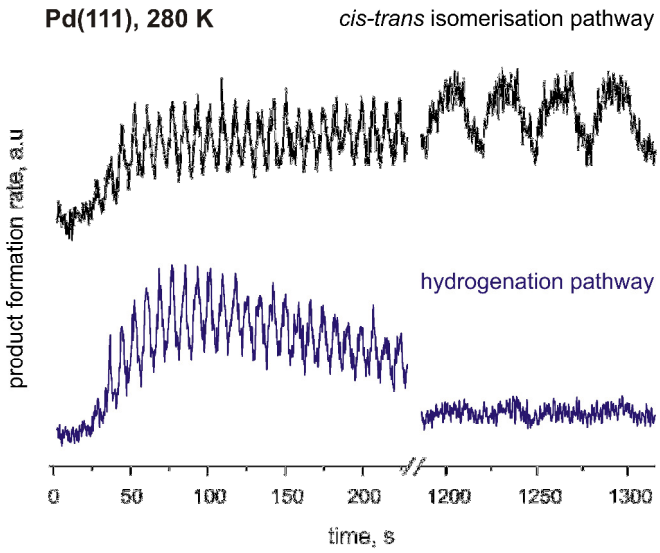

Figure S1. Isothermal pulsed molecular beam experiments on Pd(111). The evolution of the reaction rates is shown as a function of time for *cis-trans* isomerization (upper trace) and hydrogenation (lower trace) of *cis*-2-butene with D_2 at 280 K. Pd(111) was saturated first with a continuous D_2 beam to form both surface and subsurface D species and then short pulses of *cis*-2-butene were applied. Pd(111) exhibits persistent *cis-trans* isomerization activity, while initially high hydrogenation rate vanishes after depletion of subsurface D.

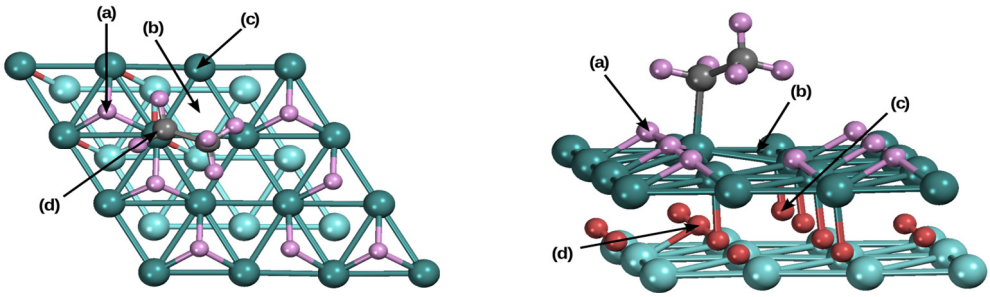

Figure S2. Initial state structure of the *subsurface-saturated* single-crystal model (see Figure 1) with adsorbed ethyl species (left panel – top view; right panel – side view). Considered are four different cases, where attacking H is initially located in one of two on-surface (a, b) or two subsurface (c, d) positions, indicated by arrows. During the reaction, H in positions (a, c, d) moves to the on-surface position (b) before attacking ethyl species. Hence, no TS structure corresponding to direct H attack from a subsurface position was found. Surface Pd – dark blue; subsurface Pd – light blue; C – gray; surface H – pink; subsurface H – red.

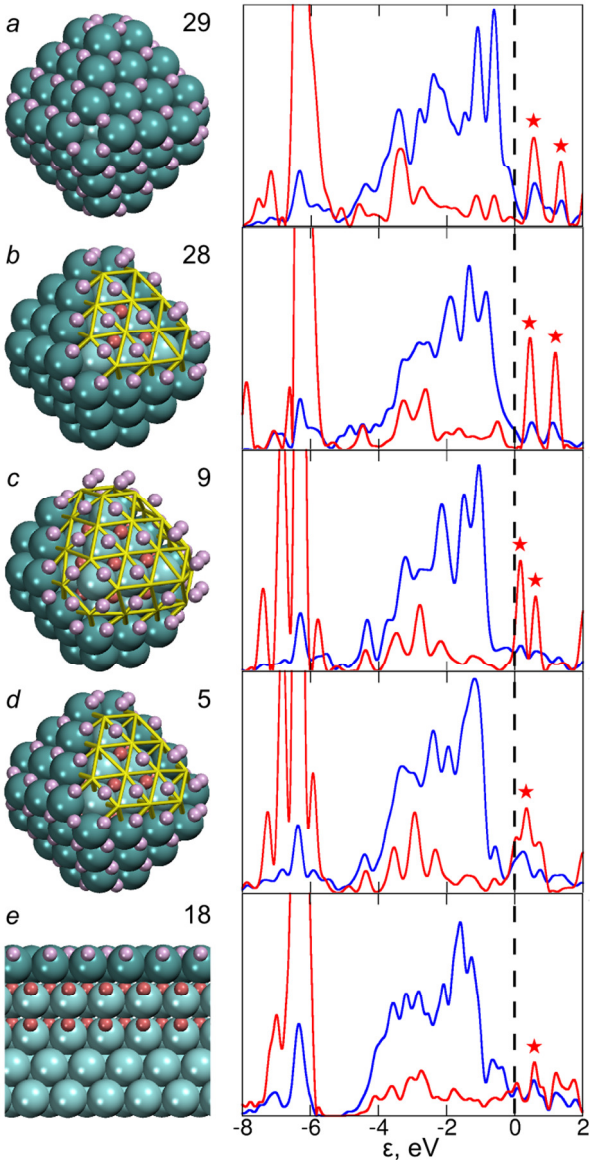

Figure S3. Structures and densities of states (DOS) of Pd_{79} NP and crystal models with varying number of H^{sub} atoms: (*a*) *surface-saturated* NP with $H^{ad}{}_{78}H^{sub}{}_{0}$; (*b*) NP with $H^{ad}{}_{23}H^{sub}{}_{3}$; (*c*) NP with $H^{ad}{}_{38}H^{sub}{}_{12}$; (*d*) *subsurface-saturated* NP with $H^{ad}{}_{78}H^{sub}{}_{24}$; *(e) subsurface-saturated×2* crystal with $H^{ad}{}_{7}H^{sub}{}_{18}$. For clarity, some surface Pd atoms Pd^{surf} are depicted as a grid connecting the atomic positions. The DOS (in arbitrary units, with respect to the Fermi energy $\varepsilon_F = 0$) are projected on selected atomic states: red – *s* state of the H^{ad} atom attacking the reacting ethyl species (×50); blue – *d* states of the three Pd^{surf} atoms forming the hollow site Pd_3, where the atom H^{ad} is located. Also shown are Gibbs activation energies (in kJ mol^{-1}) at T = 298 K of ethyl hydrogenation calculated on each model.

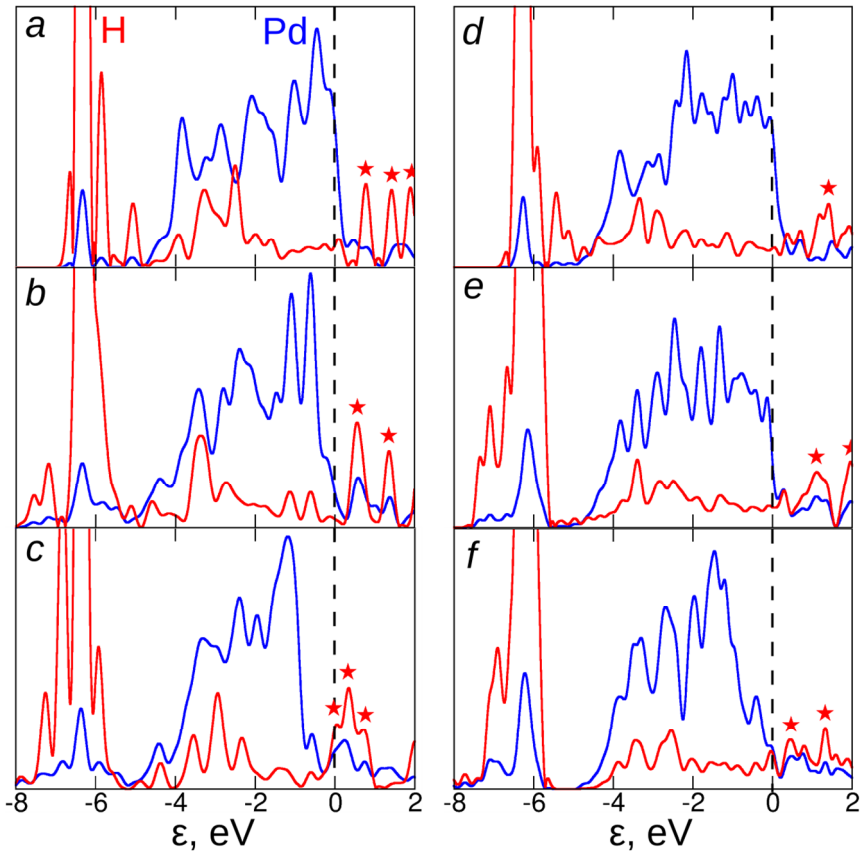

Figure S4. Electronic structure of nanoparticulate and extended Pd-H systems as a function of the hydrogen content. The density of one-electron states (in arbitrary units, with respect to the Fermi energy ε_F = 0 eV) of *(a) low-coverage*, *(b) surface-saturated*, and *(c) subsurface-saturated* NP models and *(d) low-coverage*, *(e) surface-saturated*, and *(f) subsurface-saturated* single-crystal models, projected on selected atomic states: red – H *s* states of the H^{ad} atom participating in the hydrogenation reaction (×50); blue – *d* states of the surface Pd atoms forming the hollow site Pd_3, where the atom H^{ad} is located. The H-Pd_3 antibonding states are marked by stars.

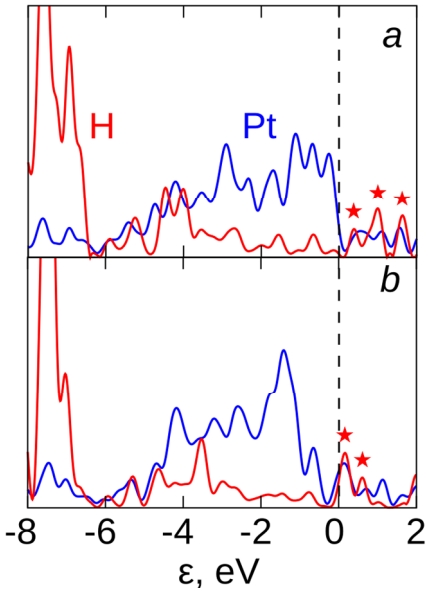

Figure S5. Dependence of the electronic structure of nanoparticulate Pt-H systems on hydrogen content. Notations are as in Figure 3: a – Pt_{79} NP saturated with adsorbed hydrogen H^{ad}, b – Pt_{79} NP saturated with both adsorbed H^{ad} and subsurface H^{sub} hydrogen. The density of states (DOS) projected on: red – *s* states of the reacting H^{ad} atom (×50); blue – *d* states of the atoms forming the hollow site Pt_3, where the atom H^{ad} is located. DOS is given in arbitrary units, with respect to the Fermi energy $\varepsilon_F = 0$ eV. The H-Pt_3 antibonding states are marked by stars.

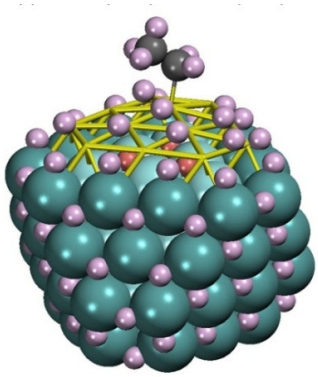

Figure S6. Sketch of the IS structure of ethyl hydrogenation on a *subsurface-saturated* NP $C_2H_5/H^{ad}{}_{78}H^{sub}{}_{24}Pd_{79}$ with high concentration of surface H^{ad} (pink) and subsurface H^{sub} (red) atoms. For clarity, Pd^{surf} atoms of one of the facets are depicted as a grid connecting the atomic positions. H atoms of ethyl are displayed in pink, C – in grey.

References

[S1] J. Libuda, I. Meusel, J. Hartmann, H.-J. Freund, *Rev. Sci. Instrum*. **2000**, *71,* 4395–4408.

[S2] B. Brandt, J.-H. Fischer, W. Ludwig, J. Libuda, F. Zaera, S. Schauermann, H.-J. Freund, *J. Phys. Chem. C* **2008**, *112*, 11408–11420.

[S3] W. Ludwig, A. Savara, K.-H. Dostert, S. Schauermann, *J. Catal*. **2011**, *284*, 148–156.

[S4] W. Ludwig, A. Savara, S. Schauermann, H.-J. Freund, *ChemPhysChem* **2010**, *11*, 2319–2322.

[S5] D. Teschner, Z. Révay, J. Borsodi, M. Hävecker, A. Knop-Gericke, R. Schlögl, D. Milroy, S. D. Jackson, D. Torres, P. Sautet, *Angew. Chem. Int. Ed*. **2008**, *47*, 9274–9278; *Angew. Chem*. **2008**, *120*, 914–918.

[S6] G. Kresse, J. Hafner, *Phys. Rev. B* **1994**, *49*, 14251–14269.

[S7] G. Kresse, J. Furthmüller, *Comput. Mater. Sci.* **1996**, *6*, 15–50.

[S8] J. P. Perdew, Y. Wang, *Phys. Rev. B* **1992**, *45*, 13244–13249.

[S9] P. E. Blöchl, *Phys. Rev. B* **1994**, *50*, 17953–17979.

[S10] G. Kresse, D. Joubert, *Phys. Rev. B* **1999**, *59*, 1758–1775.

[S11] S. Grimme, *J. Comp. Chem.* **2006**, *27*, 1787–1799.

[S12] H. A. Aleksandrov, F. Viñes, W. Ludwig, S. Schauermann, K. M. Neyman, *Chem. - Eur. J.* **2013**, *19*, 1335–1345.

[S13] J. W. Ochterski, Thermochemistry in *Gaussian*, **2000**, 1–19, www.gaussian.com/g_whitepap/thermo.htm

[S14] N. Hansen, T. Kerber, J. Sauer, A. T. Bell, F. J. Keil, *J. Am. Chem. Soc.* **2010**, *132*, 11525–11538.

[S15] H. A. Aleksandrov, G. N. Vayssilov, *Catal. Today* **2010**, *152*, 78–87.

[S16] G. Henkelman, H. Jónsson, *J. Chem. Phys*. **1999**, *111*, 7010–7022.

[S17] G. Mills, H. Jónsson, G. K. Schenter, *Surf. Sci*. **1995**, *324*, 305–337.

[S18] H. Jónsson, G. Mills, K. W. Jacobsen, in *Classical and Quantum Dynamics in Condensed Phase Simulations*, (Eds.: B. J. Berne, G. Ciccotti, D. F. Coker) World Scientific, Singapore, **1998**; p. 385.

[S19] P. Janthon, S. M. Kozlov, F. Viñes, J. Limtrakul, F. Illas, *J. Chem. Theory Comput.* **2013**, *9*, 1631–1640.

[S20] H. J. Monkhorst, J. D. Pack *Phys. Rev. B* **1976**, *13*, 5188–5192.

[S21] I. V. Yudanov, R. Sahnoun, K. M. Neyman, N. Rösch, *J. Chem. Phys*. **2002**, *117*, 9887–9896.

[S22] G. Hammond, *J. Am. Chem. Soc.* **1955**, *77*, 334–338.